J Mater Sci (2020) 55:2006–2017

Chemical routes to materials

An integrated and robust yolk–shell nanoreactor based on wrinkly silica microspheres loaded with Au nanoparticles and nested in a silica inverse opal

Yiming Zhao[1], Yingchun Guo[1], Xiaomei Wang[1,*], and Xu Zhang[1,*]

[1] *Local Joint Engineering Laboratory for Energy Conservation in Chemical Process Integration and Resources Utilization, Hebei Key Laboratory of Functional Polymers, and School of Chemical Engineering and Technology, Hebei University of Technology, Tianjin, China*

Received: 22 July 2019
Accepted: 27 September 2019
Published online: 16 October 2019

ABSTRACT

To construct secondary processes of multiscale architecturing, wrinkly silica microspheres (WSMs) are nested into the empty chamber of templated macroporous structure by using core–shell microspheres to self-assemble the colloidal crystal template and selectively removing the shells. It is a universal approach to form the binary inverse opal (IO) structures and maintain interconnected nanochannels. With gold nanoparticles loaded on the WSMs (denoted Au-WSMs@IO SiO_2) in the meantime, it has been demonstrated by the reduction of 4-nitrophenol (4-NP) that the binary IO materials (Au-WSMs@IO SiO_2) exhibited higher catalytic efficiency than simple nested microspheres (Au-WSMs) after recycling 15 times. Furthermore, it was nice to see it had excellent catalytic effect in the epoxidation of styrene. Owing to the outstanding catalytic activity, recyclability and mechanical stability of the binary IO materials, it will be a promising way to widely apply in heterogeneous catalysis.

Introduction

Design, construction and control of porous structure on micro- and nanoscale have always been an important science subject because they develop far-reaching significance on understanding structure–property relationship [1, 2]. Hierarchically porous structures have attracted tremendous interest in virtue of large accessible space, high surface area, high porosity and interconnected hierarchical porosity at different length scales [3–5]. It is a superb structure that can concurrently achieve both improved transport characteristics and maximized harnessed surface areas. The three-dimensional inverse opal (IO) structures, as typical hierarchically porous structures with micropores (< 2 nm), mesopores (2–50 nm) and macropores (> 50 nm) [6], can be synthesized by colloidal crystal templating in a relatively straightforward manner. IO materials own distinguished features, such as an open, interconnected macropore structure and nanosized wall composed of

Address correspondence to E-mail: xmwang@hebut.edu.cn; xuzhang@hebut.edu.cn

https://doi.org/10.1007/s10853-019-04093-4

micropores or mesopores, which supply multidimensional mass transport pathway, as well as minimized diffusion distance and resistance. What's more, the integrated structure of monolithic IO materials can offer excellent mechanical stability and cycling stability in reaction. Therefore, IO materials are more and more widely applied in energy storage and conversion, catalysis, batteries, adsorption, separation, gas sensing and biomedicine [6–8].

The approaches of exquisite control IO structural hierarchy in multiscale architecture are continuously developing to obtain improved performances [1]. Many advances have been made to form binary IO structures, including endeavors to embed secondary structures into the primary IO structure [9, 10]. To maintain the intrinsic interconnectivity of the primary IO frame, the secondary structure should have a comparable shape and size as the IO inner chamber. The nested species, with a smaller size than the interconnecting pore of the IO frame, will leach out through the interconnecting pore; in contrast, the nested species with a larger size than the interconnecting pore cannot be introduced into IO frame. In either case, the embedding process will disrupt the pore interconnectivity and structural hierarchy of the primary structure. To overcome the above problems, there is a novel approach of employing core–shell-structured microspheres as colloidal particles to assemble opal structures and selectively removing the shells after the formation of composite structures [11]. In this manner, colloidal particles as the secondary structures are elaborately implanted in the primary IO structures retaining the pore connectivity and structural hierarchy.

Additionally, the binary IO structure can be seen as an integrated yolk–shell structure which can effectively clear the hurdle of separation in continuous reactions. When ultrafine noble metal nanoparticles (NPs) are loaded on the nested microspheres, the binary IO materials are considered to be ideal nanoreactors because the IO structure serves as a protective shield that prevents the aggregation of nested microspheres, prohibits the leakage of catalytic core particles and allows the reactants and products to transfer through it rapidly. What's more, there is a highly notable feature that a void gap between the nested particle and IO frame is generated simultaneously, which accommodates the guest molecules in a homogeneous environment for the reaction [12–14]. And the void gap provides space for nested particles to agitate the reaction substrates, thereby forming an integrated and robust nanoreactor in series with multiple yolk–shell structures, which makes substrates repeatedly contact catalytic sites [15]. Recently, a three-dimensionally integrated yolk–shell (3D-IYS) nanoreactor was elaborately fabricated and it effectively catalyzed cascade reaction [15]. A novel structure of wrinkly silica microspheres (WSMs) with large specific surface area and center-radial large pores [16–19] has demonstrated that it could dramatically reduce the reunion of Au NPs loaded on it under high temperature, weak basic and acidic conditions [18]. The WSMs nested into IO structures are greatly helpful in establishing the structure–property relationship in the hierarchically porous catalytic reactor, which potentially obtain dual protection on alleviating aggregation of noble metal NPs in harsh environments on account of their high surface energy and extremely small size [20, 21].

In this paper, we undertake a dedicated endeavor to propose a general method to fabricate the nanoreactor with binary IO structure. The fabrication procedure is illustrated in Scheme 1. Firstly, WSMs were generated in the bicontinuous microemulsion and then functioned with amino groups by a post-grafting strategy. Secondly, amino-WSMs were decorated with Au NPs through the coordinating and electron donating effect. Thirdly, a resorcinol–formaldehyde (RF) resin layer was deposited on Au-WSMs to construct core–shell-structured Au-WSMs@RF nanospheres. The RF layer was used as a sacrificial template to form the voids between yolk and shell. Thereafter, the general scheme was employed to synthesize templated macroporous SiO_2 shell: The dispersive core–shell Au-WSMs@RF nanospheres were assembled by centrifugation to fabricate the colloidal crystal templates followed by the infiltration with precursor solution. After the conversion of precursor solution into a solid skeleton, the RF layer was removed by calcination and the nanoreactor with integrated yolk–shell structure was achieved (denoted as Au-WSMs@IO SiO_2). By comparing the efficiency of catalytic reduction of 4-NP between Au-WSMs and Au-WSMs@IO SiO_2, it could be confirmed that the movable yolks facilitate the accessibility to active sites and Au NPs can undergo harsh environments under the dual protection of WSMs yolk and templated macroporous SiO_2 shell to enhance the availability of reusing.

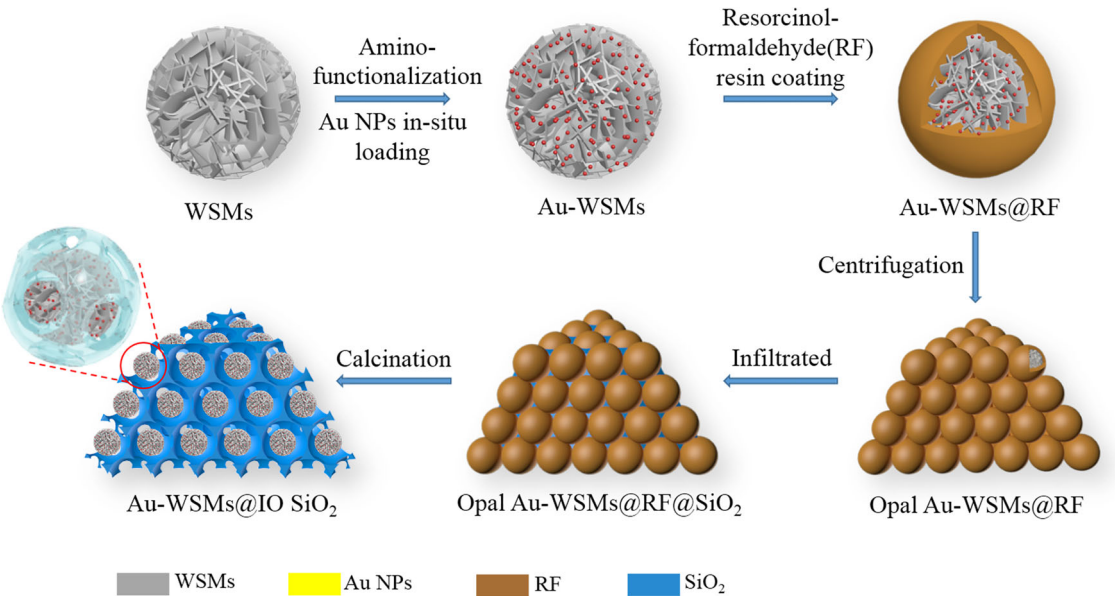

Scheme 1 Schematic synthesis of the Au-WSMs@IO SiO_2.

Experimental section

Materials

Tetraethoxysilane (TEOS, 28%), resorcinol (≥ 99.5%), formaldehyde solution (37.0% ~ 40.0%), ammonia solution ($NH_3{\cdot}H_2O$, 25% ~ 28%), urea (≥ 99.0%), cyclohexane (≥ 99.5%) and tert-Butyl hydroperoxide (TBHP) were purchased from Tianjin Fuchen Chemical Reagents Factory. Isopropyl alcohol (≥ 99.7%), absolute ethanol (≥ 99.7%) and acetonitrile (99%) were obtained from Tianjin Jindongtianzheng Precision Chemical Reagents Factory. (3-Aminopropyl) triethoxysilane (APTES, ≥ 98%) and hydrogen tetrachloroaurate (III) hydrate (Au ≥ 47.8%) were purchased from Shanghai Dibdai Chemical Technology Company. Cetyltrimethylammonium bromide (CTAB) was purchased from Tianjin Jinke Fine Chemical Research Institute. Polyvinylpyrrolidone (PVP-K30, M_w = 58,000 g mol^{-1}) and styrene were ordered from Tianjin Guangfu Fine Chemical Research Institute. Hydrochloric acid (HCl) was purchased from Beijing Chemical Works. Sodium borohydride ($NaBH_4$, 98%) and 4-nitrophenol (4-NP) were purchased from Aladdin Industrial Corporation. TEOS and styrene were purified by distillation under reduced pressure before use. All other reagents were used as received.

Preparation of WSMs

Typically, 0.5 g of CTAB and 0.3 g of urea were dissolved in 15 mL of ultrapure water and then 0.46 mL of isopropyl alcohol and 15 mL of cyclohexane were added and stirred at room temperature for 4 h to ensure that the reagents were uniformly mixed. Subsequently, 1.5 mL of TEOS was added dropwise and the mixture was heated up to 70 °C. After stirring for 16 h, the resulted emulsion mixture was centrifuged and washed with ethanol. Finally, the obtained products were redispersed in 50 mL of ethanol and 4 mL of hydrochloric acid at 70 °C for 24 h to ensure complete removal of CTAB. The prepared WSMs were collected by centrifugation and washed several times with absolute ethanol.

Synthesis of amino-WSMs

The amino-functional WSMs were achieved via a post-grafting strategy. With ultrasonication, 0.5 g of WSMs was dispersed in 100 mL of absolute ethanol. Next, 0.5 mL of APTES was dropped into the mixture and heated up to 70 °C for 8 h. Similarly, the products were collected by centrifugation and washed several times with ethanol.

Preparation of Au-WSMs

Au NPs were loaded onto WSMs via the in situ reduction method. In a typical process, 0.5 g of amino-WSMs and 0.1 g of PVP were dispersed in 180 mL of ultrapure water with ultrasonication. Under stirring, 108 mL of a fresh $HAuCl_4$ aqueous solution with concentration of 1 mg mL^{-1} was added dropwise at 30 °C. After stirring for 4 h, 18 mL of 0.1 M freshly prepared $NaBH_4$ aqueous solution was added dropwise, and the mixture was aged for 24 h. The gold-loaded products (denoted as Au-WSMs) were separated by centrifugation and washed with water.

Synthesis of Au-WSMs@RF

Typically, the Au-WSMs were dispersed in 300 mL of ultrapure water, followed by 1 g of resorcinol, 1.4 mL of formaldehyde solution and 1.4 mL of ammonia solution. Then, the temperature was raised to 50 °C and the mixture was stirred for 2 h. Finally, the obtained Au-WSMs@RF was centrifuged and washed several times with ethanol.

Fabrication of Au-WSMs@RF@IO SiO_2

By means of centrifugation, Au-WSMs@RF microspheres were integrated together as the colloid crystal template (CCT). The precursor solution was obtained by magnetic stirring of 21 mL of TEOS, 30 mL of EtOH, 4.9 mL of H_2O and 3.9 mL of HCl at 60 °C for 1 h. After cooling to room temperature, the precursor solution was fully immersed in Au-WSMs@RF and entered the interstitial space by capillary forces. The excrescent precursor solution was sucked out after half an hour. The Au-WSMs@RF@SiO_2 composite material was washed with ethanol several times and then aged at 60 °C for one hour. Repeat the above process several times. After calcining in air at 570 °C for 4 h to remove RF resin, the Au-WSMs@RF@IO SiO_2 was obtained.

Catalytic reduction of 4-nitrophenol

The catalytic performance of Au-WSMs@IO SiO_2 was investigated via the reduction of 4-nitrophenol (4-NP) to 4-aminophenol (4-AP) as a model reaction with $NaBH_4$ as reductant. Typically, 20 mg of $NaBH_4$ and 3 mL of 0.1 mM 4-NPs were added into a double-sided translucent quartz cuvette, then 0.2 mg of Au-WSMs@IO SiO_2 was quickly added to the mixture and the UV–Vis absorption spectroscopy was carried out immediately. The mixture was in situ recorded every 1 min to monitor the successive reaction progress. In order to investigate the cyclability and stability, the catalyst was separated easily through filtering after completion of the catalysis, washed with water and dried, and the above process was repeated several times.

The method to measure the amount of Au in the catalyst is as follows. Appropriate amount of Au-WSMs@IO SiO_2 was treated with nitrohydrochloric acid and HF and diluted with ultrapure water to the concentration within the standard curve range. Au(III) standard solution with different concentrations (1 ppm, 5 ppm, 10 ppm, 15 ppm and 20 ppm) was pre-prepared. After the self-checking of inductively coupled plasma optical emission spectrometer (ICP-OES Agilent 725), the absorbance of Au(III) standard solution and treated Au-WSMs@IO SiO_2 was measured in order. The amount of Au in the catalyst was directly determined by ICP-OES.

Catalytic oxidation reaction of styrene

The catalytic activity for styrene oxidation reaction of as-made Au-WSMs@IO SiO_2 was also examined. The mixture containing 1 mmol styrene and 4 ml acetonitrile was stirred at room temperature for 30 min to ensure them mixing thoroughly. Then, 0.4 ml of tert-butyl hydroperoxide (TBHP) and 0.05 g of Au-WSMs@IO SiO_2 were added into the above mixture at 80 °C in a certain time. The products of styrene oxidation reaction were analyzed by the Agilent (5977A) gas chromatography–mass spectrometer (GC–MS) using a 30 m BPX 5 column with a flame ionization detector at 250 °C.

Characterization of Au-WSMs@IO SiO_2

The diameters and zeta potentials of various microspheres were measured by Malvern Zetasizer Nano-ZS90 at room temperature with ethanol or water dispersant. Fourier transform infrared (FTIR) spectra were recorded between 4000 and 400 cm^{-1} on a Bruker VECTOR-22 spectrometer using KBr pellets. Thermogravimetric analysis (TGA) was performed on the SDT Q600 thermogravimetric instrument from room temperature to 800 °C at the rate of

10 °C min^{-1}, with a constant airflow of 100 mL min^{-1}. The Brunauer–Emmett–Teller (BET) method was used to measure the specific surface area, and all the samples were degassed at 150 °C for 10 h before measurement. Nitrogen adsorption–desorption isotherms were obtained on an ASAP 2020 M + C surface area and porosity analyzer at 77 K. The pore-size distribution was calculated by desorption isotherm by using the Barrett–Joyner–Halenda (BJH) model. The morphology of products was characterized by scanning electron microscopy (SEM) using FEI Nova Nano-SEM450 at different accelerating voltages with a concentric backscattered retractable (CBS) detector. Transmission electron microscopy (TEM) images were obtained on JEM-2100F electron microscope running at 200 kV. X-ray photoelectron spectroscopy patterns were obtained on an X-ray photoelectron spectrometer (XPS, Thermo ESCALAB-250Xi, USA). Powder X-ray diffraction (XRD) measurement was carried out on a Bruker D8 DaVinci diffractometer with Cu Kα radiation (40 kV, 150 mA), operated at a scanning rate of 12° min^{-1} in a scanning range of 2θ = 5–90°. The metal element content was conducted on an inductively coupled plasma optical emission spectrometer (ICP-OES Agilent 725). The reduction of 4-nitrophenol was monitored using a UV–Vis spectrophotometer (VARIAN CARY300) at room temperature.

Results and discussion

Preparation and characterization of nanoreactor

Initially, WSMs were generated in the bicontinuous microemulsion. It can be seen from Fig. 1a that the microspheres have the radial wrinkly structure with widened radially outward channel that guarantees large specific surface area and enhances the accessibility of precious metals inside their pores [16]. Moreover, the wrinkly channels can separate and confine precious metal NPs so as to alleviate aggregation under high temperature. In the high-resolution TEM image, it is obvious that a large number of Au NPs were tightly and uniformly immobilized on the WSMs (Fig. 2a) with a mean diameter of 3.14 nm (Fig. 2d). The result of energy-dispersive X-ray (EDX) elemental spectrum also certifies the presence of Au element (Fig. S1), and the EDX elemental mapping of N and Au reveals that $–NH_2$ and Au NPs were mainly located in WSMs (Fig. 1g–i). Then, the pre-synthesized Au-WSMs were coated with a shell of RF resin, as a consequence of which the radial wrinkly pore structure and gold nanoparticles are invisible (Fig. 1c). After the hybrid Au-WSMs@RF microspheres were gathered together by centrifugation (Fig. 1d), the precursor solution penetrated into the interstitial voids and formed ultrafine silica nanoparticles by sol–gel method. The final products of Au-WSMs@IO SiO_2 were obtained after calcination at 570 °C. From Fig. 1e and f, it is apparent that one Au-WSMs is well nested in each of the macropores to form a nanoreactor unit within templated macroporous SiO_2 which will prevent aggregation of WSMs and avert the loss of Au NPs during the catalytic process. The insets of Opal Au-WSMs@RF and Au-WSMs@IO SiO_2 show that the fabricated nanoreactors with millimeter-scale size are monolithic materials. This kind of monolithic nanoreactors with integrated yolk–shell structure not only facilitates the separation process from the reaction solution but also does not weaken the transfer capacity of substrates due to the interconnected macroporous structure and the ultrathin pore wall. Although the aggregation of Au NPs is inevitable under high temperature, the wrinkly channels and the templated macroporous SiO_2 served as barriers to protect Au NPs from harsh environmental conditions, which make the size of Au NPs increase slightly from 3.14 (Fig. 2a, d) to 4.68 nm after calcination (Fig. 2b, e). The void space between WSMs and IO SiO_2, whose average thickness was calculated to be about 52.1 nm (Fig. 2c, f), can accommodate abundant guest molecules. Moreover, the mesoporous WSMs and the open windows of templated macroporous SiO_2 make it easy and fast to transport molecules. Herein, the advantages of the binary IO structures in mass transfer are fully demonstrated by analyzing structural characteristics.

As shown in Fig. S2, the zeta potential values of WSMs, amino-functional WSMs and Au-WSMs were determined by zeta potential, which were − 16.8 mV, + 33 mV and + 14.1 mV, respectively. The surface of the silica was negative charge under such condition. After the modification of WSMs with aminopropyl groups, the potential value increased significantly and became positive. The result indicates successful functionalization. After loading Au NPs, Au-WSMs remained positive charge even though the potential value decreased because of the coordination between

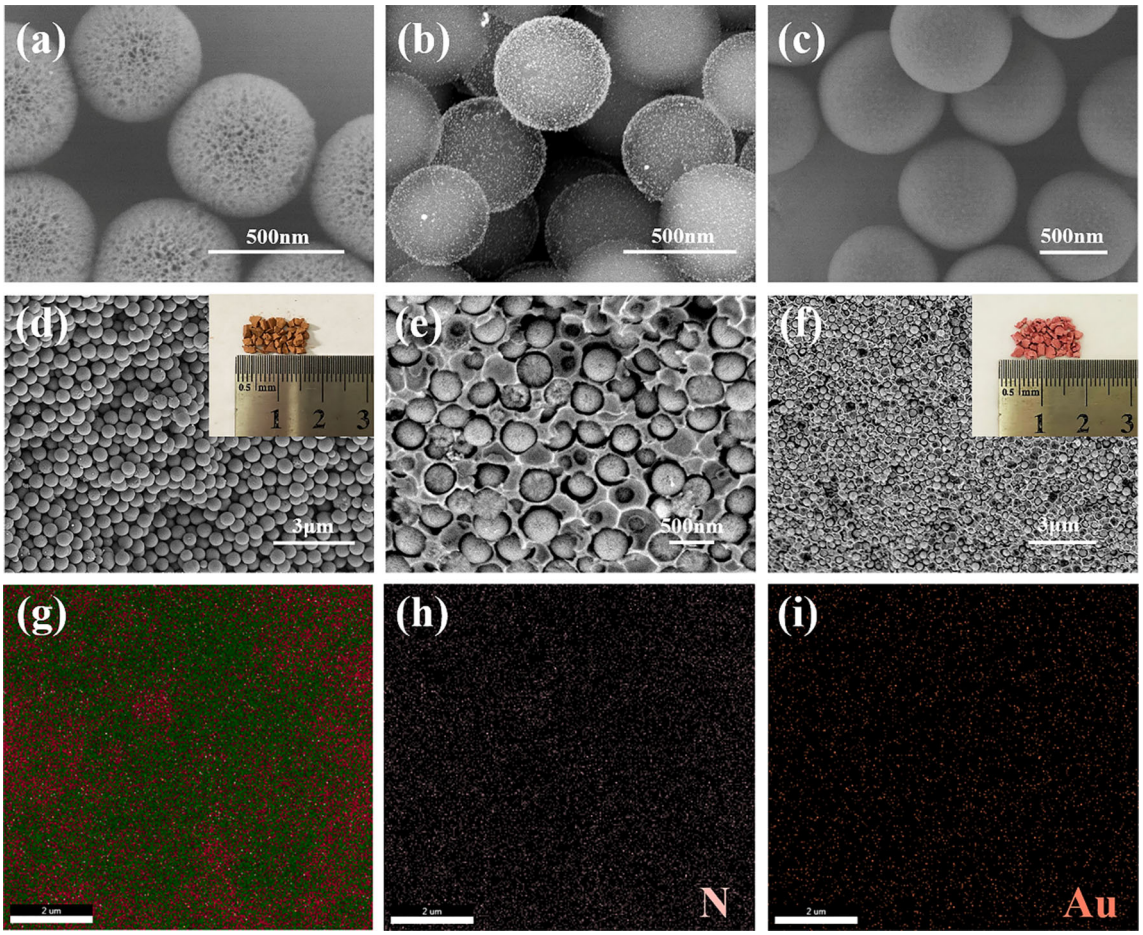

Figure 1 SEM images of **a** WSMs; **b** Au-WSMs (CBS detector at 10 kV); **c** Au-WSMs@RF; **d** opal Au-WSMs@RF; **e**, **f** Au-WSMs@IO SiO_2. (Insets are the photographs of opal Au-WSMs@RF (**d**) and Au-WSMs@IO SiO_2 (**f**), respectively.) EDX elemental mapping of overall (**g**), N (**h**) and Au (**i**) elements in Au-WSMs@IO SiO_2.

Au and N, which also facilitated heterogeneous interfacial growth of RF polymer resin with negative surface charge on the Au-WSMs due to the charge compatibility [18].

In order to make clear the compositions of relevant materials, FTIR spectra of WSMs, Au-WSMs@RF and Au-WSMs@IO SiO_2 were further characterized and are shown in Fig. 3, respectively. As displayed in the spectrum of Au-WSMs@RF, new FTIR peaks at 1618 and 1512 cm^{-1} are ascribed to C=C stretching vibrations of aromatic groups [22]. The presence of bands at 1450 and 1236 cm^{-1} is attributed to the vibration peak of $–CH_2–$ and the stretching vibration peak of C–O, respectively. The above results indicate that RF resin was immobilized and grown on the surface of Au-WSMs successfully. After calcination in air at 570 °C, the peaks disappeared manifesting that the RF resin was absolutely removed (Fig. 3c). In the three spectra, they have the peaks in common at 803, 954 and 460 cm^{-1} which are assigned to the symmetric stretching vibration (Si–O–Si), the asymmetric stretching vibration (Si–O–Si) and the Si–O–Si bending mode, respectively. The strong absorbance at 3440 and 1630 cm^{-1} corresponds to the stretching frequency of physically adsorbed water [23]. TGA curve of Au-WSMs@IO SiO_2 shows the weight loss of approximately 62%, which should be assigned to the decomposition of organic species including the RF resin and aminopropyl groups (Fig. S3).

The N_2 adsorption–desorption isotherms and pore-size distribution of the Au-WSMs and Au-WSMs@IO SiO_2 were adopted to research the pore structural evolution, as depicted in Fig. 4a and b. As can be seen, the obtained isotherms are similar to type IV isotherm curve with well-defined hysteresis loop, which is the typical curve of mesoporous materials

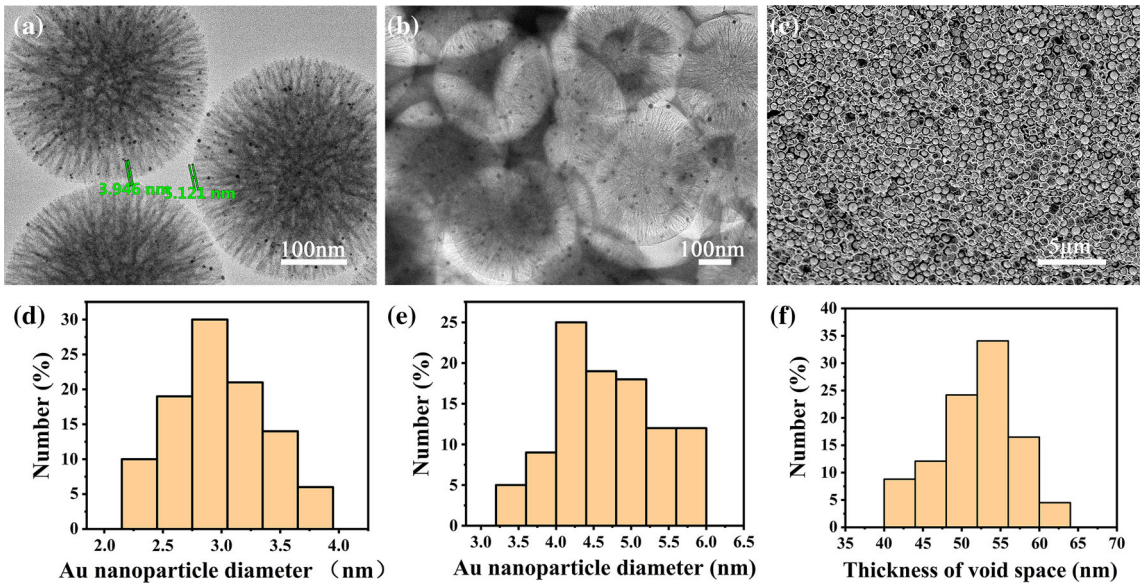

Figure 2 TEM images of **a** Au-WSMs; **b** Au-WSMs@IO SiO_2; the SEM image of (**c**) Au-WSMs@IO SiO_2; **d**, **e** the size distribution of Au NPs on Au-WSMs and Au-WSMs@IO SiO_2, respectively, estimated from the TEM images via NanoMeasurer; and **f** the size distribution of the thickness of void space between Au-WSMs and IO SiO_2 estimated from the SEM image of (**c**) via NanoMeasurer.

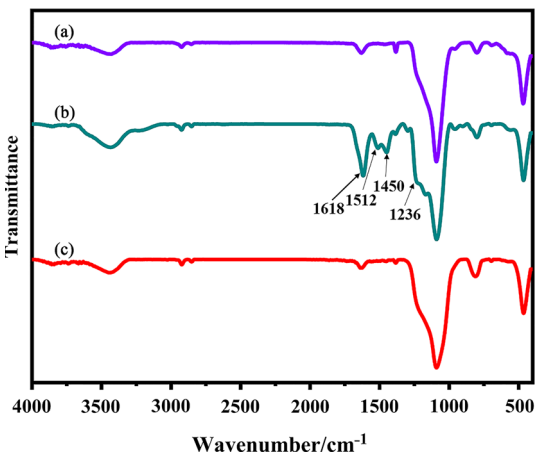

Figure 3 FTIR spectra of **a** WSMs, **b** Au-WSMs@RF and **c** Au-WSMs@IO SiO_2.

according to the IUPAC classification [24]. After the Au-WSMs were nested into templated macroporous SiO_2, the decrease in specific surface area from 431 to 320 $m^2\ g^{-1}$ could be ascribed to the lower specific surface area of templated macroporous SiO_2 (216 $m^2\ g^{-1}$, Fig. S4).

Detailed information on crystallographic composition of Au NPs loaded on the materials was obtained by XRD measurement. As exhibited in Fig. 4c, the characterized peaks at 38.22°, 44.25°, 64.68°, 77.54° and 81.72° can be indexed to the typical face-centered cubic (fcc) diffraction peaks of Au which are related to (111), (200), (220), (311) and (222), respectively (JCPDS no. 04-0784) [25]. The ratio between the intensities of the (200) and (111) diffraction peaks is much lower (0.33) than the conventional value (0.52), which demonstrates that the (111) plane is the predominant orientation [26]. Moreover, the result of XPS survey spectrum further confirms the chemical state of elements on the surface of materials. Figure 4d presents the high-resolution spectrum of Au 4*f*, 83.7 and 87.2 eV are assigned to the $4f_{7/2}$ and $4f_{5/2}$ binding energies of Au [27], which demonstrates that Au is loaded successfully. The result is in accordance with the XRD analysis.

Catalytic test

Noble metal nanoparticles with high stability and adjustable particle size, shape and composition are of great significance for the synthesis of heterogeneous catalysts with high activity, high selectivity and recyclability [28–30]. Herein, the synthesized WSMs-NH_2 with high specific surface area provides a large number of sites for the loading of noble metal nanoparticles. Its unique central, radial and wrinkly channels act as a barrier to separate noble metal nanoparticles to slow down their aggregation due to Ostwald ripening at high temperatures [18].

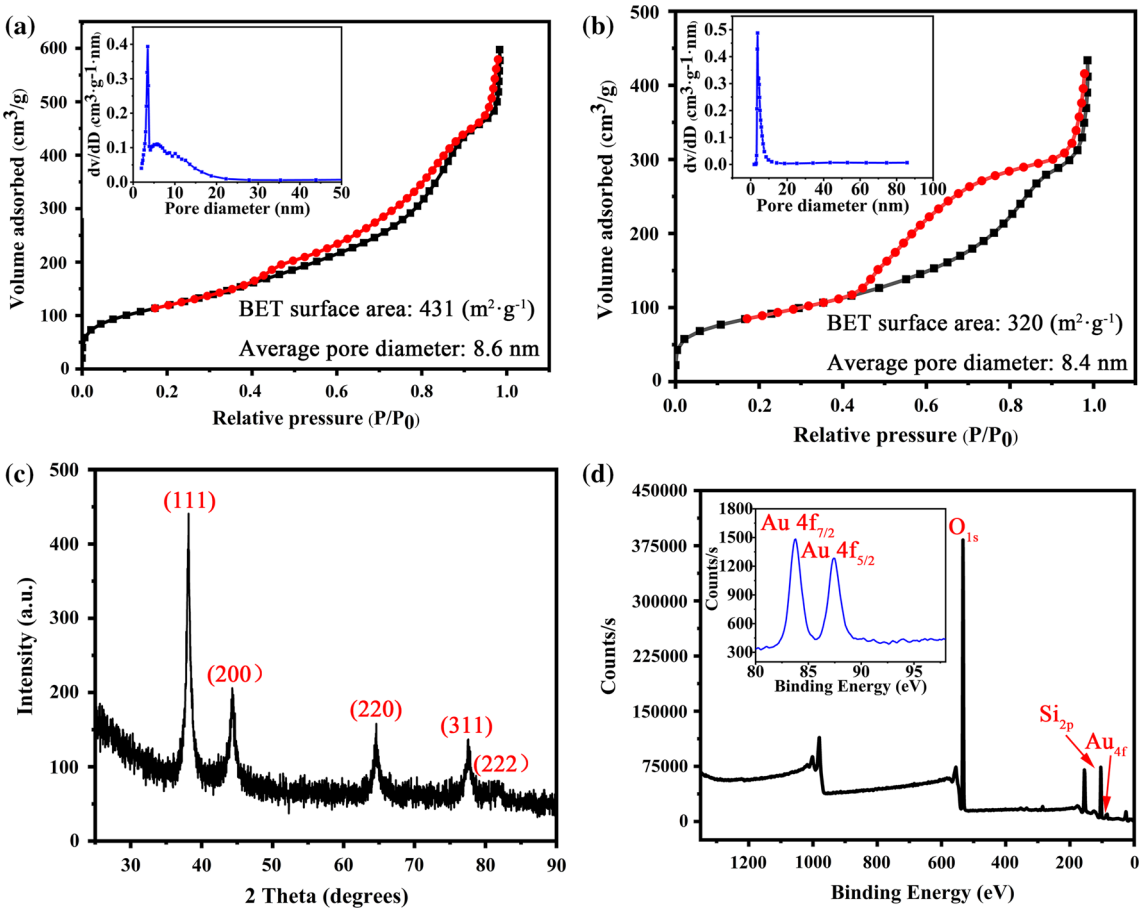

Figure 4 N_2 adsorption–desorption isotherms and pore diameter distribution (inset) of Au-WSMs (**a**) and Au-WSMs@IO SiO_2 (**b**); **c** XRD pattern of Au-WSMs@IO SiO_2; and **d** the XPS spectra of Au-WSMs@IO SiO_2 (inset is the high-resolution spectrum of Au $4f_{5/2}$ and Au $4f_{7/2}$).

Due to its high toxicity, mutagenic and carcinogenic effects on human and natural life, 4-nitrophenol (4-NP) has been identified as a priority pollutant by the US EPA [31]. Strong absorption of electronic nitro makes 4-NP more difficult to be degraded by traditional chemical or biological treatments [32]. Fortunately, Au NPs have been developed for effective catalytic reduction of 4-NP to 4-aminophenol (4-AP) in the previous reports [33]. In order to investigate the catalytic performance and stability of Au-WSMs@IO SiO_2, the typical catalytic reaction of 4-NP to 4-AP was selected with $NaBH_4$ as the reducing agent.

Generally, the amount of Au NPs on catalysts also affects the catalytic activity. Therefore, the Au contents of Au-WSMs and Au-WSMs@IO SiO_2 were measured by ICP (Table S1). In order to avoid the impact of Au content for the catalytic activity of Au-WSMs and Au-WSMs@IO SiO_2, the quantity of Au-WSMs was adjusted to make the same content of Au with Au-WSMs@IO SiO_2 in the catalytic reaction. Figure 5a and b shows successive UV–Vis absorption spectra of the reduction of 4-NP by the Au-WSMs@IO SiO_2 and Au-WSMs. The 4-NP conversion was negligible without a catalyst. Subsequently, when Au-WSMs@IO SiO_2 was introduced into the solution, the original absorption peak of 4-NP at 400 nm decreased with time which is accompanied by the simultaneous appearance of the characteristic absorption peak of 4-AP at 305 nm. The reactants could convert completely within 4 min, and the color of the solution changed from bright yellow to colorless (Fig. S6) [34]. Likewise, the catalytic reaction was completed after 4 min with the addition of Au-WSMs. The turnover frequency (TOF) of Au-WSMs@IO SiO_2 can be up to 499.7 h^{-1} despite a little bit lower than Au-WSMs that reaches up to 523.6 h^{-1} (Table S1). Au-WSMs@IO SiO_2 and Au-WSMs feature slight

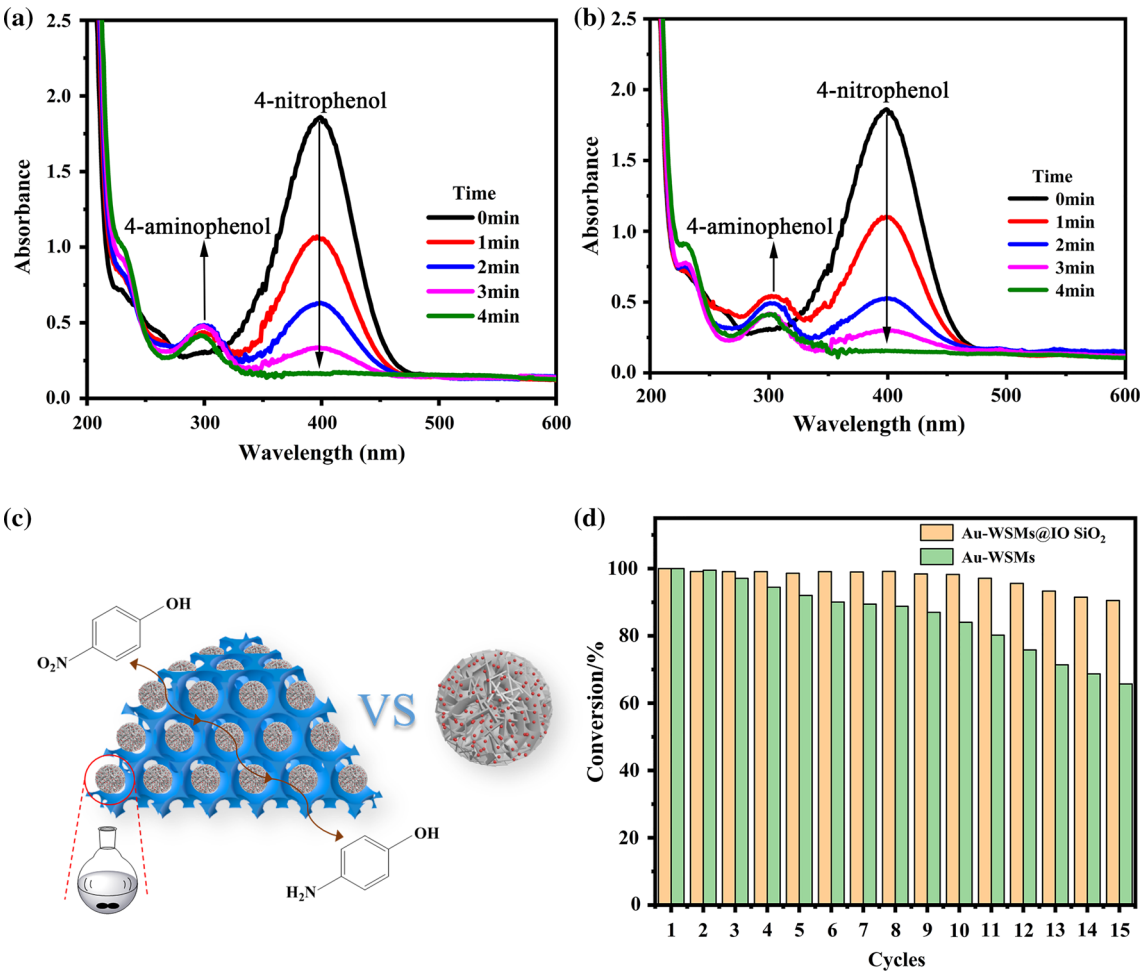

Figure 5 UV–Vis spectra of the 4-NP reduction catalyzed by Au-WSMs@IO SiO_2 (**a**) and Au-WSMs (**b**); **c** schematic illustration of Au-WSMs@IO SiO_2 and Au-WSMs; and **d** conversion of 4-NP in 15 successive cycles of reduction with catalysts.

differences in rate constant k, which are 15.4×10^{-3} s^{-1} and 17.9×10^{-3} s^{-1}, respectively (Fig. S6). Considering the same dosage of the two catalysts, the catalytic efficiency of Au-WSMs should be better because it has no shell barrier and the contact with the substrate could be direct. However, it is highly desirable to see that catalytic activity has no significant difference. The similar catalytic efficiency should be attributed to the advantages of the hierarchical binary IO structure. Significantly, the Au-WSMs@IO SiO_2 shows a remarkably higher activity than other Au catalysts under similar conditions (Table S2), suggesting a general excellent performance of WSMs@IO SiO_2 for supporting metal NPs. The continuously interconnected frame allows reactants to repeatedly contact catalytic sites through pore windows. Of particular note is that the movable nested yolks stir the guest molecules accommodated in the macropore. Accordingly, the stirring action provides a homogeneous environment for the reaction and allows sufficient contact between catalytic sites and reactants. The agitated WSMs yolk and protective templated macroporous SiO_2 shell work together to implement real reactors and guarantee good catalytic performance.

For industrial applications, the improvement in reaction rate, recyclability and stability will produce higher benefits. Figure 5d shows the recyclable reduction of 4-NP in the presence of Au-WSMs@IO SiO_2 and Au-WSMs. Au-WSMs@IO SiO_2 exhibits high catalytic performance as the conversion rate of 4-NP remained above 90% within 4 min even after 15 successive cycles. In comparison, the conversion rate of 4-NP in the presence of Au-WSMs is only about 65% after reusing in 15 successive reactions. This difference in recyclability stability is due to the loss of

Table 1 Conversion and selectivity versus time for styrene epoxidation

Time (h)	Conversion (%)	Selectivity of styrene epoxide (%)	Selectivity of benzaldehyde (%)
6	38.84	38.23	38.80
12	89.83	62.02	33.85

Au NPs and Au-WSMs in the recycling process. In addition, the Au content of Au-WSMs dropped from 2.90 to 1.42 wt%, while that of Au-WSMs@IO SiO_2 slightly decreased from 1.16 to 1.11 wt% after recycling 15 times. This result clearly demonstrates that templated macroporous structure prevents the escape of Au NPs and improves recovery efficiency. Furthermore, Au-WSMs could not be collected from the solution as easily and rapidly as Au-WSMs@IO SiO_2, which reveals the benefits of monolithic catalysts in catalyst separation. Based on the above analysis, it can be manifested that integrated heterogeneous catalysts offer excellent mechanical stability and recyclability for the reaction.

Styrene epoxide is an industrially versatile intermediate, mainly synthesized by catalytic epoxidation reaction [35–40]. In addition to the reduction of 4-nitrophenol, it has been demonstrated that Au-WSMs@IO SiO_2 is capable of being a quite effective catalyst for the epoxidation of styrene. TBHP was chosen as an oxidant (Fig. 6). As shown in Table 1, with the prolonged reaction time, the conversion of styrene increased from 38.84% (6 h) to 89.83% (12 h); meanwhile, the selectivity rose from 38.23% (6 h) to 62.02% (12 h). Those results show the catalytic activity of Au-WSMs@IO SiO_2 is higher than other catalysts reported in previous papers [36, 39] in styrene oxidation. The epoxidation performance confirmed that Au-WSMs@IO SiO_2 acted as an excellent catalyst in the epoxidation of styrene and the result is highly ascribed to the combination of ultrafine pore shell and ultrasmall Au NPs.

Conclusion

In summary, the binary IO structures were fabricated by a facile strategy that a secondary structure was nested into the primary IO structure and the feasibility of their application as high-performance catalysts was further investigated. To implement nested structures, novel nanostructured Au-WSMs@RF as core–shell colloidal microspheres were employed to form CCT and the RF shells were selectively removed. The resulted binary IO structures (Au-WSMs@IO SiO_2) not only ensure the accessibility to the active sites and superior mass transport but also conspicuously suppress the aggregation of noble metal nanoparticles and enhance the recyclability of materials, which lead to the high catalytic activity of 90% after 15 times recycles in the reduction of 4-NP and high conversion in catalytic styrene epoxidation. Accordingly, the high catalytic activity together with easy collection of the binary IO nanoreactors makes it advantageous in the catalytic application. More importantly, the binary IO nanoreactors can be extended to load other noble metal nanoparticles, which would possess broad application in nanocatalysis.

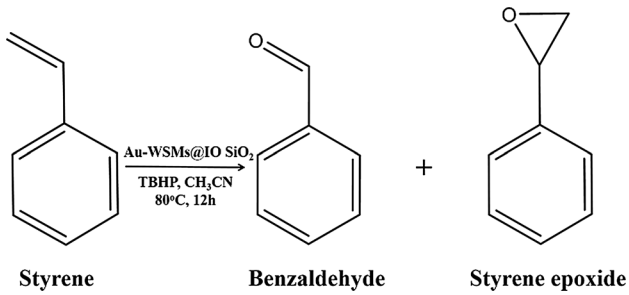

Figure 6 Reaction formula of the epoxidation of styrene.

Acknowledgements

This work was supported by grants from the National Natural Science Foundation of China (Grant No. 51573038, 51403049 and 50903027) and the Natural Science Foundation of Hebei Province (Nos. E2016202261 and E2017202036).

Compliance with ethical standards

Conflict of interest The authors have no conflicts of interest related to this work.

Electronic supplementary material: The online version of this article (https://doi.org/10.1007/s108

53-019-04093-4) contains supplementary material, which is available to authorized users.

References

[1] Wu D, Xu F, Sun B, Fu R, He H, Matyjaszewski K (2012) Design and preparation of porous polymers. Chem Rev 112:3959–4015

[2] Yeo SJ, Choi GH, Yoo PJ (2017) Multiscale-architectured functional membranes utilizing inverse opal structures. J Mater Chem A 5:17111–17134

[3] Kong X, Wu C, Feng L, Qu J, Liu P, Wang X, Zhang X (2017) Silica-based hierarchical porous janus microcapsules: construction and supported Au nano-particles catalyst inside. Chem Commun 53:8054–8057

[4] Stein A, Li F, Denny NR (2008) Morphological control in colloidal crystal templating of inverse opals, hierarchical structures, and shaped particles. Chem Mater 20:649–666

[5] Stein A, Wilson BE, Rudisill SG (2013) Design and functionality of colloidal-crystal-templated materials: chemical applications of inverse opals. Chem Soc Rev 42:2763–2803

[6] Sun MH, Huang SZ, Chen LH, Li Y, Yang XY, Yuan ZY, Su BL (2016) Applications of hierarchically structured porous materials from energy storage and conversion, catalysis, photocatalysis, adsorption, separation, and sensing to biomedicine. Chem Soc Rev 47:3479–3563

[7] Yang XY, Chen LH, Li Y, Rooke JC, Sanchezc C, Su BL (2017) Hierarchically porous materials: synthesis strategies and structure design. Chem Soc Rev 46:481–558

[8] Su BL, Sanchez C, Yang XY (2011) Self-formation phenomenon to hierarchically structured porous materials. Hierarchically structured porous materials: from nanoscience to catalysis, separation, optics, energy, and life science. Wiley, Hoboken

[9] Yeo SJ, Kang H, Kim YH, Han S, Yoo PJ (2012) Layer-by-layer assembly of polyelectrolyte multilayers in three-dimensional inverse opal structured templates. ACS Appl Mater Interfaces 4:2107–2115

[10] Cho CY, Moon JH (2011) Hierarchically porous TiO_2 electrodes fabricated by dual templating methods for dye-sensitized solar cells. Adv Mater 23:2971–2975

[11] Rhee DK, Jung B, Kim YH, Yeo SJ, Choi SJ, Rauf A, Han S, Yi GR, Lee D, Yoo PJ (2014) Particle-nested inverse opal structures as hierarchically structured large-scale membranes with tunable separation properties. ACS Appl Mater Interfaces 6:9950–9954

[12] Liu J, Qiao SZ, Chen JS, Lou XW, Xing X, Lu GQ (2011) Yolk/shell nanoparticles: new platforms for nanoreactors, drug delivery and lithium-ion batteries. Chem Commun 47:12578–12591

[13] Priebe M, Fromm KM (2015) Nanorattles or yolk-shell nanoparticles-what are they, how are they made, and what are they good for? Chem -Eur J 21:3854–3874

[14] Purbia R, Paria S (2015) Yolk/shell nanoparticles: classifications, synthesis, properties, and applications. Nanoscale 7:19789–19873

[15] Guo Y, Feng L, Wang X, Zhang X (2019) Integration of yolk–shell units into robust and highly reactive nanoreactor: a platform for cascade reactions. ChemComm 55:3093–3096

[16] Moon DS, Lee JK (2012) Tunable synthesis of hierarchical mesoporous silica nanoparticles with radial wrinkle structure. Langmuir 28:12341–12347

[17] Yu H, Zhang Q, Dahl M, Joo JB, Wang X, Wang L, Yin Y (2017) Dual-pore carbon shells for efficient removal of humic acid from water. Chem-Eur J 23:16249–16256

[18] Du X, Zhao C, Luan Y, Zhang C, Jaroniec M, Huang H, Zhang X, Qiao SZ (2017) Dendritic porous yolk@ordered mesoporous shell structured heterogeneous nanocatalysts with enhanced stability. J Mater Chem A 5:21560–21569

[19] Shen D, Chen L, Yang J, Zhang R, Wei Y, Li X, Li W, Sun Z, Zhu H, Abdullah AM, Al-Enizi A, Elzatahry AA, Zhang F, Zhao D (2015) Ultradispersed palladium nanoparticles in three-dimensional dendritic mesoporous silica nanospheres: toward active and stable heterogeneous catalysts. ACS Appl Mater Interfaces 7:17450–17459

[20] Wu Q, Xiong J, Zhang Y, Mei X, Wei Y, Zhao Z, Liu J, Li J (2019) Interaction-induced self-assembly of Au@La_2O_3 core-shell nanoparticles on $La_2O_2CO_3$ nanorods with enhanced catalytic activity and stability for soot oxidation. ACS Catal 9:3700–3715

[21] Liu Z, Che R, Elzatahry AA, Zhao D (2014) Direct imaging Au nanoparticle migration inside mesoporous silica channels. ACS Nano 8:10455–10460

[22] Trick KA, Saliba TE (1995) Mechanisms of the pyrolysis of phenolic resin in a carbon/phenolic composite. Carbon 33:1509–1515

[23] Li R, Song H, Wang G, Chen J (2018) Efficient and reusable SBA-15-immobilized Brønsted acidic ionic liquid for the ketalization of cyclohexanone with glycol. RSC Adv 8:7179–7185

[24] Zhao D, Yang P, Chmelka BF, Stucky GD (1999) Multiphase assembly of mesoporous–macroporous membranes. Chem Mater 11:1174–1178

[25] Xia Q, Su D, Yang X, Chai F, Wang C, Jiang J (2015) One pot synthesis of gold hollow nanospheres with efficient and reusable catalysis. RSC Adv 5:58522–58527

[26] Jena BK, Raj CR (2007) Synthesis of flower-like gold nanoparticles and their electrocatalytic activity towards the

oxidation of methanol and the reduction of oxygen. Langmuir 23:4064–4070

[27] Zhang Y, Park SJ (2017) Au–Pd bimetallic alloy nanoparticle-decorated $BiPO_4$, nanorods for enhanced photocatalytic oxidation of trichloroethylene. J Catal 355:1–10

[28] Xu Y, Chen L, Wang X, Yao W, Zhang Q (2015) Recent advances in noble metal based composite nanocatalysts: colloidal synthesis, properties, and catalytic applications. Nanoscale 7:10559–10583

[29] Wu B, Zheng N (2013) Surface and interface control of noble metal nanocrystals for catalytic and electrocatalytic applications. Nano‘ Today 8:168–197

[30] Schauermann S, Nilius N, Shaikhutdinov S, Freund HJ (2013) Nanoparticles for heterogeneous catalysis: new mechanistic insights. Acc Chem Res 46:1673–1681

[31] Sun SP, Lemley AT (2011) p-Nitrophenol degradation by a heterogeneous fenton-like reaction on nano-magnetite: process optimization, kinetics, and degradation pathways. J Mol Catal A-Chem 349:71–79

[32] Wang Y, Xie Y, Sun H, Xiao J, Cao H, Wang S (2015) Hierarchically shape-controlled mixed-valence calcium manganites for catalytic ozonation of aqueous phenolic compounds. Catal Sci Technol 6:2918–2929

[33] Zhang D, Zhang G, Zhang L (2017) Multi-shelled $FeCo_2O_4$ hollow porous microspheres/CCFs magnetic hybrid and its dual-functional catalytic performance. Chem Eng J 330:792–803

[34] Hayakawa K, Yoshimura T, Esumi K (2003) Preparation of gold-dendrimer nanocomposites by laser irradiation and their catalytic reduction of 4-nitrophenol. Langmuir 19:5517–5521

[35] Wang X, Liang Z, Zhang F, Yang L, Xu S (2013) Enhanced catalytic performances of Ag nanoparticles supported on layered double hydroxide for styrene epoxidation. J Mater Sci 48:5899–5903. https://doi.org/10.1007/s10853-013-7385-7

[36] Gu Y, Li C, Bai J, Zhang Y, Wang J (2016) The construction of Au/carbon nanocomposite material, characterization and their application in catalytic reaction of styrene epoxidation. J Clust Sci 27:1147–1158

[37] Liu B, Wang P, Lopes A, Jin L, Zhong W, Pei Y, Suib SL, He J (2017) Au-carbon electronic interaction mediated selective oxidation of styrene. ACS Catal 7:3483–3488

[38] Saikia M, Kaichev V, Saikia L (2016) Gold nanoparticles supported on nanoscale amine-functionalized MIL-101(Cr) as a highly active catalyst for epoxidation of styrene. RSC Adv 6:106856–106865

[39] Zhao D, Xiong X, Qu CL, Zhang N (2014) Remarkable enhancement in Au catalytic utilization for liquid redox reactions by galvanic deposition of Au on Cu nanoparticles. J Phys Chem C 118:19007–19016

[40] Zhao X, Wang P, Ma Z, Pei Y (2019) Phenyl ring transfer mechanism of styrene selective oxidation to phenyl acetaldehyde on gold catalysts from density functional theory (DFT) studies. J Phys Chem C 123:1710–1719